The Effects of Waves on the Meridional Thermal Structure of Jupiter's Stratosphere

Richard G. Cosentino[a,c], Thomas Greathouse[b], Amy Simon[c], Rohini Giles[b],
Raúl Morales-Juberías[d], Leigh N. Fletcher[e], Glenn Orton[f]

[a] *"Department of Astronomy, University of Maryland, College Park, MD 20742 (U.S.A)*
[b] *Southwest Research Institute, San Antonio, TX 78238 (U.S.A.)*
[c] *Solar System Exploration Div., NASA/GSFC, Greenbelt, MD 20771 (U.S.A.)*
[d] *Physics Department, New Mexico Institute of Technology, Socorro, NM 87801 (U.S.A.)*
[e] *School of Physics and Astronomy, University of Leicester, University Road, Leicester LE1 7RH (U.K.)*
[f] *Jet Propulsion Laboratory, California Institute of Technology, 4800 Oak Grove Drive, Pasadena, CA 91109 (U.S.A.)*

Abstract

A thermal oscillation in Jupiter's equatorial stratosphere, thought to have ∼4 Earth year period, was first discovered in 7.8 μm imaging observations from the 1980s and 1990s. Such imaging observations were sensitive to the 10–20 hPa pressure region in the atmosphere. More recent 7.8 μm long-slit high-spectroscopic observations from 2012–2017 taken using the Texas Echelon cross-dispersed Echelle Spectrograph (TEXES), mounted on the NASA Infrared Telescope Facility (IRTF), have vertically resolved this phenomenon's structure, and show it spans a range of pressure from 2–20 hPa. The TEXES instrument was mounted on the Gemini North telescope in March 2017, improving the diffraction-limited spatial resolution by a factor of ∼2.5 compared to that offered by the IRTF. This Gemini spatial scale sensitivity study was performed in support of the longer-termed Jupiter monitoring being performed at the IRTF. We find that the spatial resolution afforded by the smaller 3-m IRTF is sufficient to spatially resolve the 3-D structure of Jupiter's equatorial stratospheric oscillation by comparing the thermal retrievals of IRTF and Gemini observations. We then performed numerical simulations in a general circulation model to investigate how the structure of Jupiter's stratosphere responds to changes in the latitudinal extent of wave forcing in the troposphere. We find our simulations produce a lower limit in meridional wave forcing of ±7° (planetocentric coordinates) centered about the equator. This likely remains constant over time in order to produce off-equatorial thermal oscillations at ±13°, consistent with observations spanning nearly four decades.

Keywords: Jupiter, Stratosphere Oscillation, Infrared Observations,

---

Email address: `richard.cosentino @ nasa.gov` (Richard G. Cosentino)

Preprint submitted to Elsevier *September 29, 2020*

1. Introduction

NASA's Infrared Telescope Facility (IRTF) atop Maunakea was used to observe Jupiter through the 1980s and 1990s. These observations revealed a semi-regular thermal oscillation in stratospheric equatorial and off-equatorial brightness temperatures with a ∼4 Earth year period (Leovy et al., 1991; Orton et al., 1991). This phenomenon was named the Quasi-Quadrennial Oscillation (QQO) and is thought to be analogous to Earth's Quasi-Biennial Oscillation (QBO), the wave-forced descent of vertically stacked east-west equatorial stratospheric jets over time (Friedson, 1999; Li & Read, 2000; Baldwin et al., 2001; Cosentino et al., 2017). Re-analysis of data taken in the 1980s and 1990s has found the period of Jupiter's equatorial stratospheric oscillation (JESO[1]) to be more variable than previously thought (Antuñano et al., 2020). The Composite Infrared Spectrometer (CIRS) aboard the Cassini spacecraft revealed the presence of a strong jet in Jupiter's stratosphere near 4 hPa, which coincided with a relative temperature maximum phase of the QQO or JESO (Flasar et al., 2004; Antuñano et al., 2020). Previous studies of this region in Jupiter's atmosphere have utilized the thermal wind equation to indirectly infer atmospheric jets from observations (Flasar et al., 2004; Simon-Miller et al., 2006). Building on work by Cosentino et al. (2017), this paper aims to understand the meridional and vertical temperature structure associated with the JESO from utilizing unique observations and wave-forced numerical model simulations of Jupiter's stratosphere.

Ground-based observations of Jupiter from NASA's IRTF made with the Texas Echelon Cross Echelle Spectrograph (TEXES) instrument (Lacy et al., 2002) have sampled multiple points of the JESO cycle from 2012 to 2017 (Fletcher et al., 2016; Cosentino et al., 2017; Melin et al., 2018). TEXES' high spectral resolution allows for the retrieval of temperatures that are spatially resolved, both horizontally and vertically, and have revealed the presence of several equatorial relative thermal maxima and minima in the JESO's cycle. The equatorial vertically stacked extrema descend, appearing to alternate position with each other, tracking the JESO's evolution over the pressure range of 2–20 hPa in Jupiter's stratosphere for many years (Leovy et al., 1991; Orton et al., 1991; Friedson, 1999; Simon-Miller et al., 2006; Cosentino et al., 2017; Melin et al., 2018; Giles et al., 2020; Antuñano et al., 2020)

Cosentino et al. (2017) showed how parameterized gravity wave effects attributed to convection near the equator in a general circulation model (GCM) could reproduce many observed QQO properties, including the four-year period and relationships between equatorial and off-equatorial temperatures. Their modeled meridional and vertical temperature fields were qualitatively similar to the TEXES observations at different phases in the oscillation. They used a stochastic gravity wave drag (GWD) forcing that had a Gaussian taper centered on the equator with a meridional full-width at half maximum (FWHM)

---

[1] **JESO does not imply the phenomenon's frequency in years.**

on an idealized equatorial jet. These values were varied as part of an extensive parameter space exploration to best reproduce the observations.

In this paper, we specifically focus on the spatial extent of relative temperature extrema from ground-based observations, how GCM parameters related to wave forcing impact the equatorial QQO temperature structure, and explore the relationships between equatorial and off-equatorial temperatures. To aid in our study of the spatial extent of the JESO, we present high spatial resolution TEXES observations from the 8.1-meter Gemini North telescope. These observations were conducted to investigate whether previous analysis of the lower spatial resolution observations taken with TEXES mounted on the IRTF was hampered by data obtained at the 3-meter telescope. In Section 2 we describe the TEXES observations at IRTF and Gemini North. In Section 3 we describe our analysis of the observations. Section 4 presents numerical experiments and the comparison of model output to observations. In Section 5 we discuss the results of our paper and conclusions are presented in Section 6.

2. Observations

The TEXES instrument (Lacy et al., 2002) was used to take high-resolution mid-infrared observations of Jupiter on thirteen observing runs between 2012 and 2017. Giles et al. (2020) Section 2 provides additional information about the observations and data reduction, while Section 3 details the radiative transfer modeling. Here we present information pertinent to our specific study of the spatial structure of Jupiter's stratosphere.

TEXES is a cross-dispersed grating spectrograph, covering wavelengths of 4.5–25 μm in the mid-infrared. The instrument has a scan-map mode, allowing the slit to be stepped across an extended object. In order to study Jupiter's stratospheric temperatures, the instrument's highest spectral resolution was used (R=80,000) and the observations were centered at 1247.5 cm^{-1} (8.02 μm), with a spectral bandpass of $\sim$7 cm^{-1}. This allows six strong CH_4 ν_4 emission lines to be resolved; together, these emission lines are sensitive to the temperature profile in the 0.1–30 hPa pressure region. The scan-map mode was used to build up full longitudinal coverage on each observing run, resulting in three-dimensional spectral datacubes of the planet.

The observations of Jupiter were analyzed with the data-reduction pipeline described in Lacy et al. (2002). Observations from several consecutive nights were combined to produce a single cylindrical map with 2° latitude[2] bins, which were then zonally averaged. These zonally averaged TEXES spectra were analyzed using a radiative transfer and retrieval code Greathouse et al. (2011) to extract the vertical stratospheric temperature profile as a function of latitude. The line-by-line radiative transfer code calculates the top-of-atmosphere radiance for given atmospheric profile and the optimal estimation retrieval code uses a Levenberg-Marquardt approach to fit the modeled spectrum to the observed

---

[2] All observation latitudes are in planetocentric coordinates unless otherwise noted.

spectrum. For each of the TEXES spectra, the vertical temperature profile in the stratosphere was allowed to vary to fit the observations. Figure 1 in Giles et al. (2020) shows an a priori atmospheric profile and example quality of the fit of November 2015 TEXES dataset. The formal error bars on the temperature retrievals are ∼1.5 K between ±30° latitude, but we adopt a more conservative error of 2 K to include systematic effects for all of the data.

One of these thirteen observing runs was conducted at Gemini North, while the other twelve took place at NASA's IRTF. After many years of tracking the JESO with TEXES at the IRTF, we conducted similar observations with TEXES mounted on Gemini North **(abbreviated here after as Gemini)** to confirm that the spatial resolution afforded by TEXES on the IRTF was capable of fully resolving the JESO's spatial structure. Moving to the larger aperture 8-m class Gemini telescope allowed for approximately 2.5 times better spatial resolution than that achievable on the 3-m IRTF (as spatial resolution depends linearly on the telescope diameter for a given wavelength). Observations made at Gemini used the same spectral setup and observing mode as those at the IRTF, and the same data reduction and temperature retrieval process was applied to all data.

When TEXES was moved from IRTF to Gemini, certain aspects to perform a consistent spatial sensitivity study with the same instrument at different observatories are now discussed. The plate scale in m/radian at the slit is equal to the effective focal length of the telescope + our fore-optics, which is equal to the f# at the slit times the telescope diameter. Since we modified the fore-optics to properly couple TEXES to the Gemini telescope, keeping the f# at the slit constant, the plate scale changed by a factor of 8m/3m. As a result the slit width projected onto the sky decreased by a factor of 3/8. The diffraction limit decreased by the same factor. Gemini is able to perform fast tip/tilt correction allowing for diffraction limited performance at 8 μm (image motion being the dominant seeing effect at this wavelength), significantly smaller than the $0.5''$ (arcseconds) wide slit used for these observations. The seeing on Mauna Kea is approximately equal to the diffraction limit of the IRTF at 8 μm and the two are less than the $1.4''$ wide slit employed for our observations at the IRTF. Thus the image performance on both telescopes is approximately diffraction limited and more importantly, slit width limited in the case of our study. This is different from the situation with a visible wavelength instrument, in which the spatial resolution is set by the seeing disk, which requires a larger slit relative to diffraction on a bigger telescope.

Figure 1 shows how the Jupiter's stratospheric temperatures we retrieved vary over the 2012–2017 time period. The three lines show the zonally-averaged retrieved temperatures near 14 hPa at three different latitudes: 13°S, 0°, and 13°N. The Gemini observation is highlighted by the grey shaded region. The sinusoidal-like oscillation with time is characteristic of the JESO and the 2012–2017 time period covers approximately 1.5 cycles. The equatorial and off-equatorial temperatures near 14 hPa exhibit strongly anti-correlated temperature variations consistent with prior observations sensitive to pressures of 10–20 hPa (Leovy et al., 1991; Orton et al., 1991; Friedson, 1999; Simon-Miller et al., 2006). The magnitude of the JESO signals at 14 hPa is at least ±6 K away from the median temperature for both the equator and off-equatorial latitudes with a period slightly longer than ∼4.5 Earth years (Giles et al., 2020). Since we are not exploring the variability in the period of JESO, as done in Antuñano et al. (2020), we use QQO throughout the paper when referring to the oscillation's frequency of four Earth years.

The long-term behavior of the QQO, as seen in the TEXES observations, has previously been studied by Cosentino et al. (2017) and Giles et al. (2020). In this paper, we initially focus on observing runs conducted in 2017; these consist of three IRTF observing runs (January, May, and July 2017) and the one Gemini observing run (March 2017). The tight clustering of these observing runs and the slow evolution of the QQO allows us to investigate this time period in detail. Observations from the IRTF in 2013 were compared to 2017 data since they represent two separate QQO relative minima phases at 14 hPa. We additionally analyzed 2015 when the QQO was in the opposite relative maximum phase.

Figure 2 panel (a) shows retrieved equatorial vertical temperature profiles for the QQO relative maximum and minimum in 2015 and 2017, respectively. The reference temperature profile is the average of the maximum and minimum in the time series at each pressure level. This reference approximates a median temperature, which is favored in lieu of the mean to avoid over-weighting closely spaced observations of a non-uniformly sampled time series (e.g. the numerous observations in 2017). Vertical profile deviations for the QQO relative maximum phase at 14 hPa are shown in Figure 2 panel (b) displaying a mirrored vertical structure to those in panel (c), which is in the opposite QQO relative minimum phase at the same pressure. The three profiles in Figure 2 panel (c) show good agreement over the time spanned by data acquired from different observatories. The pressure range between 11–16 hPa is where we focus our analysis of the QQO's meridional structure, and is indicated by the shaded region of interest (ROI) in Figure 2 panel (c).

Figure 2 panel (c) indicates that equatorial temperatures in 2017 between 10–20 hPa are consistent with each other when considering our estimated 2 K uncertainty. The descent rate of the QQO thermal extrema from Cosentino et al. (2017) of 0.05 cm s^{-1} translates to roughly 1.3 km/month, which corresponds to ∼7 km of vertical displacement from January to July. This translation is a fraction of the ∼25 km scale height in Jupiter's stratosphere at these pressures. The slow descent rate and agreement of data demonstrate there is very little vertical evolution in the QQO over these observations, and provides the best opportunity to investigate the meridional temperature structure of Jupiter's stratosphere at this time.

Retrieved temperatures in the pressure range 1–30 hPa for latitudes $\pm 25^\circ$ from IRTF and Gemini data in January and March 2017 are shown in Figure 3 panels (a–b), respectively. Contours are spaced at 2 K intervals, approximating our adopted uncertainty, and the dashed horizontal line at 30 hPa represents our high pressure limit. There is good agreement in the 2D retrieved temperature contour magnitude and spacing, especially near the equator at 14 hPa, indicated by y-axis tick marks. Figure 3 panel (c) introduces a different representation of the data by showing a comparison of the meridional temperature profile for the Gemini data along with profiles from the preceding and following IRTF observations in 2017. The meridional profiles virtually overlap each other and adjacent pressures exhibit a similar morphology (see appendix Figure A.1). In the next section, we will analyze the meridional profiles in greater detail to quantify the structure of the QQO as seen from the different observatories.

3. QQO Meridional Width from IRTF and Gemini

This section focuses on the meridional structure of the observations shown in Figure 3 panel (c) and additionally analyzed data from February 2013 and April 2015. We developed two fitting methods to quantify the QQO's structure between 11–16 hPa for these observations; representing opposite relative extrema. At first glance, the retrieved temperatures at the relative QQO minima in Figure 3 panel (c) somewhat resemble a sine curve. We used a non-linear least squares fitting procedure to model the meridional shape of retrieved temperatures between 11°S–11°N. The "best fit" converged solution optimized model free parameters for the temperature data; amplitude, phase, offset, and wavelength. We also quantified the meridional width by fitting a Gaussian curve to the same data using a similar method with different free parameters; amplitude, baseline, and standard deviation. This two-pronged approach allows for the comparison of the half-wavelength from the sine curve fit to the FWHM of the Gaussian fit to quantify the equatorial structure of the QQO, which as shown in Figure 4 is essentially measuring the same physical quantity.

Figure 4 chronologically shows retrieved temperature profiles at 14 hPa from different QQO phases along with their respective sine curve and Gaussian fits. The Gemini observation taken with increased spatial resolution is shown in Figure 4 panel (c) with its sinusoidal (dashed) and Gaussian (solid) fits. Figure 4 panel (a) shows data and fits from the previous relative minimum and bears a strikingly similar appearance to panel (c). The opposite relative maximum phase in 2015 is shown in Figure 4 panel (b). All of the sine half-wavelength and Gaussian FWHMs for Figure 4 are listed in Table 1. We also present results from the other observations in 2017 at pressures within the ROI in Figure 2 panel (c).

The sine curve half-wavelengths and Gaussian FWHMs of the March Gemini data are consistent with fits from IRTF observations taken before and after when one considers the 2° latitude bins of the spectral data. Gemini data acquired with increased spatial resolution do not show any obvious or significant departures from the other low-resolution IRTF observations. Both fitting methods quantify the meridional width of the QQO minimum phase to be ∼12° latitude; ±6° from the equator. This is further supported by analysis of the 2013 QQO relative minimum phase at 14 hPa which found a similar meridional width ∼12° latitude. Our dataset only contains a single QQO relative maximum at 14 hPa and fits produce a slightly smaller meridional width for this phase but there is not enough variation to speculate that they are significantly different at this time. The sine fit for 16 hPa IRTF data from January 2017 is our sole noticeably different fitted value found in Table 1. We attribute this anomaly to fitting transitions between different QQO extrema phases which is elaborated in the appendix.

We computed the standard deviation of the fits at each pressure for results in Table 1. We also wanted to estimate uncertainties associated with the fitting methods by varying the latitude domain by 2° on either side of the 11°S–11°N nominal case shown in Figure 4 and in Table 1. There generally was less than ∼1° change in fitted widths for 9°S–9°N and 13°S–13°N from the values reported in Table 1. Considering the 2° latitude bins, a 1° change in the fitted meridional extent of the QQO's equatorial structure is insignificant and our results are largely not sensitive to small changes in the number of data used to generate fits. This stems from both fitting methods concentrating on data at the equator where adding or removing a single pair of points at the end of the fits are not a driving factor in determining the converged solutions for the different functional form fits. We also resampled the Gemini data in 0.5° bins, taking advantage of the telescope's increased resolution, and found no significant changes in the thermal structure or fits to the QQO's meridional extent.

There are three main results from analysis in this section: (1) The two fitting methods mostly found similar meridional widths for pressures between 11–16 hPa for the 2017 data. (2) These were acquired at two different telescopes over a relatively short time span (compared to the QQO four-year period), with Gemini taken at a higher spatial resolution than IRTF, and there is no significant change in the ∼12° meridional structure found. (3) Two different fitting methods found similar structure for data representing a previous QQO equatorial minima phase in 2013 at 14 hPa. The consistency of our results from these analyses support that the meridional width of retrieved QQO temperature structure are well-resolved at both telescopes and the results of our fitting methods are generally robust.

We applied these fitting methods to the entire times series of data shown in Figure 1 and discuss those results later and in the Appendix; see Figure A.2.

4. QQO Modeling

We used the Explicit Planetary Isentropic Code (EPIC, Version 3.8 Dowling et al. (1998)) GCM to simulate the QQO in Jupiter's stratosphere. EPIC integrates the hydrostatic, primitive equations on an oblate sphere, and it can be initialized with a zonal wind profile in the horizontal direction and with observed temperature profiles in the vertical. A brief summary of the model, domain, and parameters of Cosentino et al. (2017) is provided in the next paragraph.

Cosentino et al. (2017) used a stochastic gravity wave drag (GWD) module to randomly sample momentum flux amplitudes and phase speeds of waves to force the QQO. The method combined computational efficiency (Eckermann, 2011) with latent heat release from convective effects in a GCM (Alexander & Pfister, 1995) to simulate a source of waves from moist convection based on observations (Gierasch et al., 2000; de Pater et al., 2019). The period of the oscillation is primarily determined by the stress term from breaking waves, forcing the opposite jets to descend, which correspond to oscillations in the region's temperatures via thermal wind balance.

In this study, we specifically investigated how the horizontal extent of wave drag and initialized Gaussian jet width affected the modeled stratospheric temperature amplitudes and meridional structure. The modeling presented here, as in Cosentino et al. (2017), utilizes a zonal forcing wave parameterization in a 2D GCM domain of latitude and pressure. The model meridional horizontal resolution of 1.1°_{g} extending between $\pm 45^{\circ}_{g}$ planetographic latitude[3] and the 60 vertical layers from 1000 to 0.01 hPa were unchanged from Cosentino et al. (2017). An idealized equatorial Gaussian jet was initialized with a velocity range of 81-79 ms^{-1} from the model bottom layer to the top, respectively, providing a starting vertical shear condition. A time step of 40 seconds was used and the model was run for 20 Earth years allowing for the QQO to mature and stabilize such that we could analyze the third oscillation. The top six layers of the model were set as "sponge" layers to dampen numerical instabilities from developing near the model upper boundary. All other parameter values and details of the GCM to reproduce the QQO not specifically mentioned, such as hyperviscosity, etc. are provided by Cosentino et al. (2017).

The FWHM of the GWD and the QQO jet were changed by 1°_{g} increments spanning 2-10°_{g} in latitude within EPIC. Those two parameters were varied exploring values away from the "best" case in Cosentino et al. (2017), which had FWHMs of 5°_{g} for the GWD and an initialized QQO jet of 8°_{g}. Our GCM horizontal resolution is nearly twice that from our observations such that EPIC can sufficiently resolve the impact of parameters changes and their effect on simulated QQO properties when compared to TEXES data. Cases that had GWD widths **centered at the equator** of $\leq 2^{\circ}_{g}$ did not produce a QQO, and cases with GWD $\geq 8^{\circ}_{g}$ were numerically unstable[4]; these are not shown. All simulations presented in this paper were numerically stable and had multiple QQO periods of ~4.0 ±0.2 years.

We developed analyses that allowed us to compare different QQO phases from TEXES observations to the results of our parameter space exploration of EPIC simulations. Figure 5 panel (a) shows the meridional retrieved temperature profiles for different observed QQO relative extrema; equatorial temperature maximum in 2015 and minimum in 2017 at 14 hPa. Underneath that, Figure 5 panel (c) shows the deviation of these profiles from the average of the opposite phases per latitude; essentially displaying the QQO amplitude. We applied this same analysis to the different QQO phases in a simulation with GWD and jet FWHMs of 5°_{g} and 8°_{g}, respectively, shown in Figure 5 panel (b). **The resulting simulated QQO amplitudes versus latitude shown in Figure 5 bear similarities to our observational analysis in shape and signature location of off-equatorial latitudes. It is worth noting that**

---

[3] EPIC planetographic latitudes, noted by subscript "g", are converted to planetocentric when compared to observations.

[4] See Appendix Figure A.3 for more information on the numerical stability of specific cases.

while the simulated QQO amplitudes have magnitudes less than those found in observations, our model is able to reproduce the QQO's spatial signatures. The analyses presented in Figure 5 allows us to quantify characteristics in the observed QQO and identify trends in EPIC simulations as model parameters changed.

Figure 6 panel (a) shows simulated QQO temperature amplitudes at 14 hPa, calculated in the same manner as those in Figure 5 panels (c-d). In this panel, we show results from a constant jet FWHM of 8°_{g} for different GWD meridional forcing widths. These results numerically confirm the theoretical relationship between the width of wave forcing and its impact on the amplitude of the stratospheric oscillation (Andrews et al., 1987; Friedson, 1999). Figure 6 panel (a) also shows that the predicted latitude of the anti-correlated off-equatorial QQO signal, designated as ϕ^{*}, increases with the width of wave forcing (Andrews et al., 1987; Friedson, 1999). Observations dating back to 1980 consistently find that this off-equatorial signal is maximum at $\phi^{*}=\pm 13^{\circ}$, in planetocentric coordinates (Leovy et al., 1991; Orton et al., 1991; Friedson, 1999; Cosentino et al., 2017; Antuñano et al., 2020). Simulations with GWD FWHMs $>8^{\circ}_{g}$ (7° planetocentric coordinates) were numerically unstable; see appendix Figure A.3. Figure 6 panel (b) shows QQO temperature amplitudes from simulations where the GWD FWHM was held constant at 5°_{g} (4.4° planetocentric coordinates) for different jet widths. There is no significant impact of varying the FWHM of the jet for the same width of wave forcing on QQO temperature amplitudes or the location of ϕ^{*}.

We applied the same sinusoidal and Gaussian fitting analyses to simulated QQO temperatures from EPIC. Gaussian FWHM values of the modeled equatorial temperature structure at 14 hPa for the QQO minimum phase for simulations in Figure 6 panel (a) were $\sim$8-10°, while the sine curve half-wavelengths were slightly larger, $\sim$9-11°. At the simulated QQO maximum phase, we found that both Gaussian FWHM and sine curve widths were $\sim$10-13°. The widths of both QQO phases are similar or just below those found from analysis of the QQO from TEXES observations. The results from measuring adjacent pressure levels in EPIC yielded similar results. The more interesting results from our simulations that we will discuss in the next section are the trends in amplitude and the location ϕ^{*} as the wave forcing is increased, and what those potentially imply about the actual temperatures and winds in Jupiter's stratosphere and the source of waves driving the QQO.

5. Discussion

Results from our analysis of meridional structure of the QQO from TEXES observations at different telescopes found similar widths via two different fitting methods. The higher-resolution data obtained from Gemini are consistent with all of the other IRTF observations supporting the fact that the QQO is well resolved by the IRTF. As future observations continue to monitor the QQO's evolution, there is no significant scientific advantage gained by conducting QQO monitoring observations at increased spatial resolutions higher than those achieved with the combination of the IRTF and TEXES.

Figure A.2 shows that the sine curve fitting routine does not converge on half-wavelengths at times when the QQO is not at a relative maxima or minima. Instead, very large half-wavelengths are found at transitions or mid-points between opposite QQO phases. On the other hand, Gaussian FWHMs are fairly consistent for all of the observations at different QQO phases and transitions between relative extrema. This could result from the behavior shown in Figure 5 panel (b) where the sine curve fit is more appropriate for the relative minimum phase, but not necessarily the relative maximum phase.

The location of ϕ^* is related to the width of wave forcing and the response of stress in the stratosphere to produce a secondary circulation. Observations over the last four decades consistently indicate $\phi^*=\pm 13^\circ$ (Cosentino et al., 2017; Antuñano et al., 2020). Figure 5 panels (b) and (d) show that the simulated QQO amplitudes peak at the equator but also at slightly lower latitudes than $\phi^*=\pm 13^\circ$. Figure 6 panel (a) shows that a GWD FWHM of 6.1° (or $\pm 7^\circ_g$) produces a QQO amplitude pattern that is in agreement with the location of ϕ^* in Figure 5 is consistent with observations. High-frequency gravity waves from convection are more favorable as the main source of momentum driving the QQO when compared to planetary waves because the latter easily become equatorially trapped, such as the eastward propagating Kelvin wave observed in the New Horizons flyby in 2007 (Simon et al., 2015). That wave only spanned the equator by $\pm 2^\circ$ and had a phase velocity of 80 ms^{-1}, which both rule it out as a major source of momentum driving the QQO for two reasons. First, its width is much less than $\pm 6.1^\circ$ needed to generate the off-equatorial signal at ϕ^* seen in observations. Second, the relatively low phase speed confines the wave very close to the equator (Orton et al., 2020). Such a wave located at a latitude of 8°N would require phase speeds >200 ms^{-1}, but there is no observational evidence of planetary waves in such regions with these properties.

Naturally, the planetary wave features near $\pm 7^\circ$ come to mind as candidates to provide QQO momentum at higher latitudes, but as previously stated, their low phase speeds rule out scenarios of wave propagation and interaction at the equator and higher altitudes. Additionally, their larger horizontal wavelengths imply large vertical structure, perhaps 2-3 scale heights (30–60 km). The QQO region spans approximately 100 km in altitude and the ability of waves so vertically extended to interact with shear zones spanning distances less than their vertical wavelengths make it more likely for them to reflect or be evanescent in this region. High-frequency gravity waves from convection, like those parameterized in our QQO simulations, are still the most likely candidate to provide the majority of necessary forcing because they can have relatively high phase speeds and are not trapped as strongly towards the equator as planetary waves. Computer models are emerging that fully resolve horizontal and vertical wind structure and waves on gas-giant planets, and they are spontaneously producing jet banding and stratospheric oscillations (Showman et al., 2019; Young et al., 2019; Bardet et al., 2021). As with Earth's QBO, the QQO could require a combination of large- and small-scale waves in order to reproduce all of its observed properties and structure of Jupiter's stratosphere (Dunkerton, 1985; Li & Read, 2000).

Figures 5 and 6 demonstrate how our simulations fall short in reproducing the observed magnitude of QQO amplitudes at the equator and ϕ^*, but there may be an explanation in the results of our meridional width fitting shown in Figure A.2. The thermal wind relates the meridional gradient in temperature to a vertical gradient in zonal velocity. It therefore could be that our simulations have the correct forcing width based on the location of ϕ^*, but are unable to reproduce the observed thermal amplitudes because of limitations to horizontal and vertical resolutions in GCMs. Figure A.3 shows that we can not simply increase GWD forcing to obtain higher QQO amplitudes before numerical instabilities develop from vertical layers merging and crossing each other. We also found that increasing the GCM's spatial resolution results in similar numerical instabilities. It is possible that the lower EPIC QQO amplitudes are the result of lower temperature gradients resolved in the model as compared to those that actually exist in Jupiter's stratosphere. Specifically, the dual eastward jets at 7°S and 7°N could have significant vertical structure and would create temperature gradients not realized in our simulations, but previous efforts to incorporate more realistic winds ended up not producing successful QQOs.

More detailed analysis of datasets like TEXES could study subtleties in temperature gradients in efforts to investigate vertical wind structure near the equator. Advances in thermal-wind applications combined with data taken at sub-millimeter wavelengths provide unique opportunities to study this region of Jupiter's atmosphere (Marcus et al., 2019).

6. Conclusions

1. The TEXES instrument at IRTF is fully capable of resolving the spatial structure of Jupiter's QQO/JESO; confirmed by observational analysis finding similar ∼12° meridional widths of Gemini North data taken with increased spatial resolution.
2. The meridional structure of stratospheric temperatures centered about the equator was found to have a common FWHM of ∼12° for pressures spanning 10–20 hPa for different JESO phases. Transitions between opposite phases may be more difficult to analyze because of quickly evolving temperature gradients.
3. The width of wave forcing supplying momentum to JESO directly impacts the location of anti-correlated off-equatorial temperature signals at ϕ^*; which for almost four decades has been observed at ±13° planetocentric latitude. The consistent location of $\phi^*=\pm 13°$ is best supported by wave forcing originating from below with a FWHM of at least ∼7° centered at the equator.

Acknowledgement

Richard Cosentino's research was supported by an appointment to the NASA Postdoctoral Program at the NASA Goddard Space Flight Center, administered by Universities Space Research Association under contract with NASA. Thomas Greathouse was a visiting astronomer at the Infrared Telescope Facility, which is operated by the University of Hawaii under contract NNH14CK55B with the National Aeronautics and Space Administration. Thomas Greathouse retrieved, reduced, and modeled data (available upon request) with support from NASA PAST grant NNX14AG34G. Glenn Orton was supported by grants from the National Aeronautics and Space Administration to the Jet Propulsion Laboratory, California Institute of Technology. Leigh Fletcher was supported by a Royal Society Research Fellowship and European Research Council Consolidator Grant (under the European Union's Horizon 2020 research and innovation programme, grant agreement No 723890) at the University of Leicester.

References

Alexander, M. J., & Pfister, L. 1995, Geophysical Research Letters, 22, 2029

Andrews, D., Holton, J., & Leovy, C. 1987, Middle Atmosphere Dynamics (Cambridge University Press)

Antuñano, A., Cosentino, R. G., Fletcher, L. N., et al. 2020, Nature Astronomy, 9

Baldwin, M. P., Gray, L. J., Dunkerton, T. J., et al. 2001, Reviews of Geophysics, 39, 179

Bardet, D., Spiga, A., Guerlet, S., et al. 2021, Icarus, 354, 114042

Cosentino, R. G., Morales-Juberías, R., Greathouse, T., et al. 2017, Journal of Geophysical Research: Planets, n/a, 2017JE005342

de Pater, I., Sault, R. J., Moeckel, C., et al. 2019, The Astronomical Journal, 158, 139

Dowling, T. E., Fischer, A. S., Gierasch, P. J., et al. 1998, Icarus, 132, 221

Dunkerton, T. J. 1985, Journal of Atmospheric Sciences, 42, 1151

Eckermann, S. D. 2011, Journal of Atmospheric Sciences, 68, 1749

Flasar, F. M., Kunde, V. G., Achterberg, R. K., et al. 2004, Nature, 427, 132

Fletcher, L. N., Greathouse, T. K., Orton, G. S., et al. 2016, Icarus, 278, 128

Friedson, A. J. 1999, Icarus, 137, 34

Gierasch, P. J., Ingersoll, A. P., Banfield, D., et al. 2000, Nature, 403, 628

Giles, R., Greathouse, T., Cosentino, R., Orton, G., & Lacy, J. 2020, Icarus, 350, 113905

Greathouse, T. K., Richter, M., Lacy, J., et al. 2011, Icarus, 214, 606

Lacy, J. H., Richter, M. J., Greathouse, T. K., Jaffe, D. T., & Zhu, Q. 2002, The Publications of the Astronomical Society of the Pacific, 114, 153

Leovy, C. B., Friedson, A. J., & Orton, G. S. 1991, Nature, 354, 380

Li, X., & Read, P. L. 2000, Planetary and Space Science, 48, 637

Marcus, P. S., Tollefson, J., Wong, M. H., & de Pater, I. 2019, Icarus, 324, 198

Melin, H., Fletcher, L., Donnelly, P., et al. 2018, Icarus, 305, 301

Orton, G. S., Friedson, A. J., Caldwell, J., et al. 1991, Science, 252, 537

Orton, G. S., Tabataba-Vakili, F., Eichstädt, G., et al. 2020, Journal of Geophysical Research: Planets, n/a, e2019JE006369, e2019JE006369 2019JE006369

Showman, A. P., Tan, X., & Zhang, X. 2019, The Astrophysical Journal, 883, 4

Simon, A. A., Li, L., & Reuter, D. C. 2015, Geophysical Research Letters, 42, 2612

Simon-Miller, A. A., Conrath, B. J., Gierasch, P. J., et al. 2006, Icarus, 180, 98

Young, R. M., Read, P. L., & Wang, Y. 2019, Icarus, 326, 225

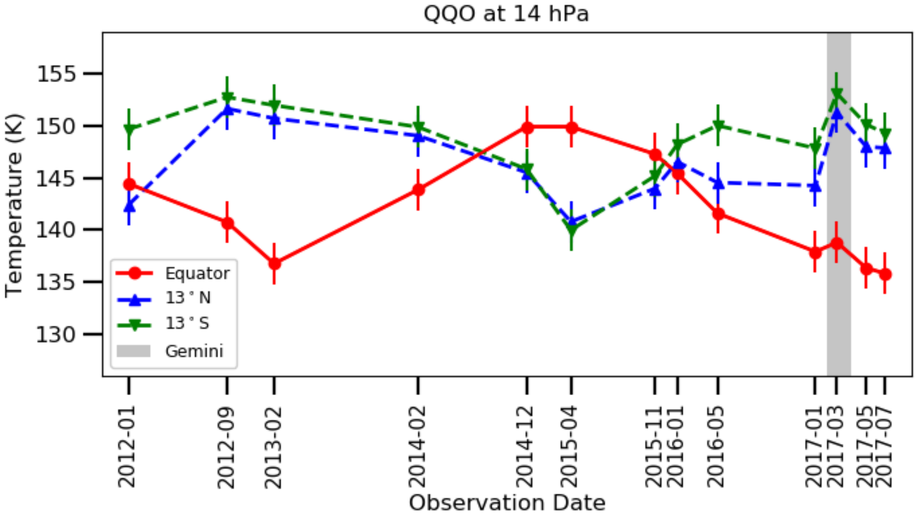

Figure 1: Equatorial (solid red) and off-equatorial (dashed blue and green) retrieved temperatures from TEXES at IRTF and Gemini (March 2017 shaded region). Variations of the equatorial temperature near 14 hPa are anti-correlated with temperatures observed at ±13° planetocentric latitude.

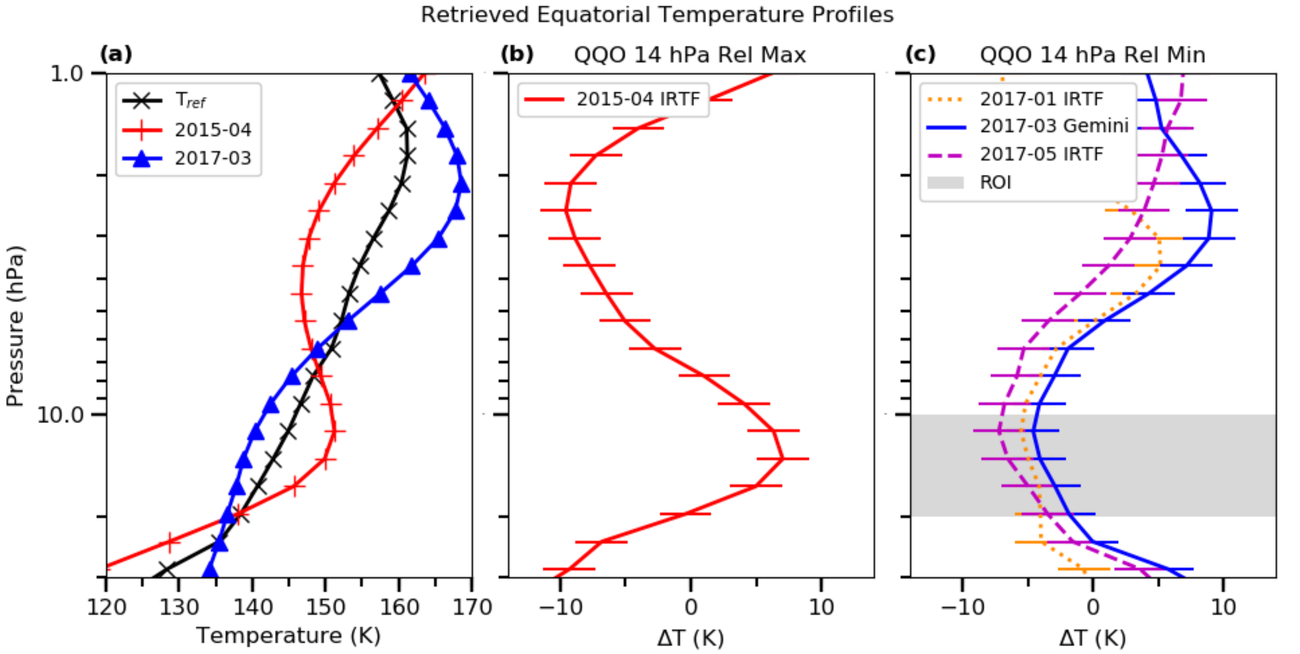

Figure 2: Panel (a) retrieved equatorial temperature profiles for QQO relative maximum and minimum. The reference temperature profile approximates the median (see details Section 2). Deviations from the reference at QQO equatorial relative maxima and minima phases are shown in (b) and (c), respectively. Panel (c) shows three profiles and a shaded region corresponding to the pressure range we analyzed to investigate the QQO's spatial structure.

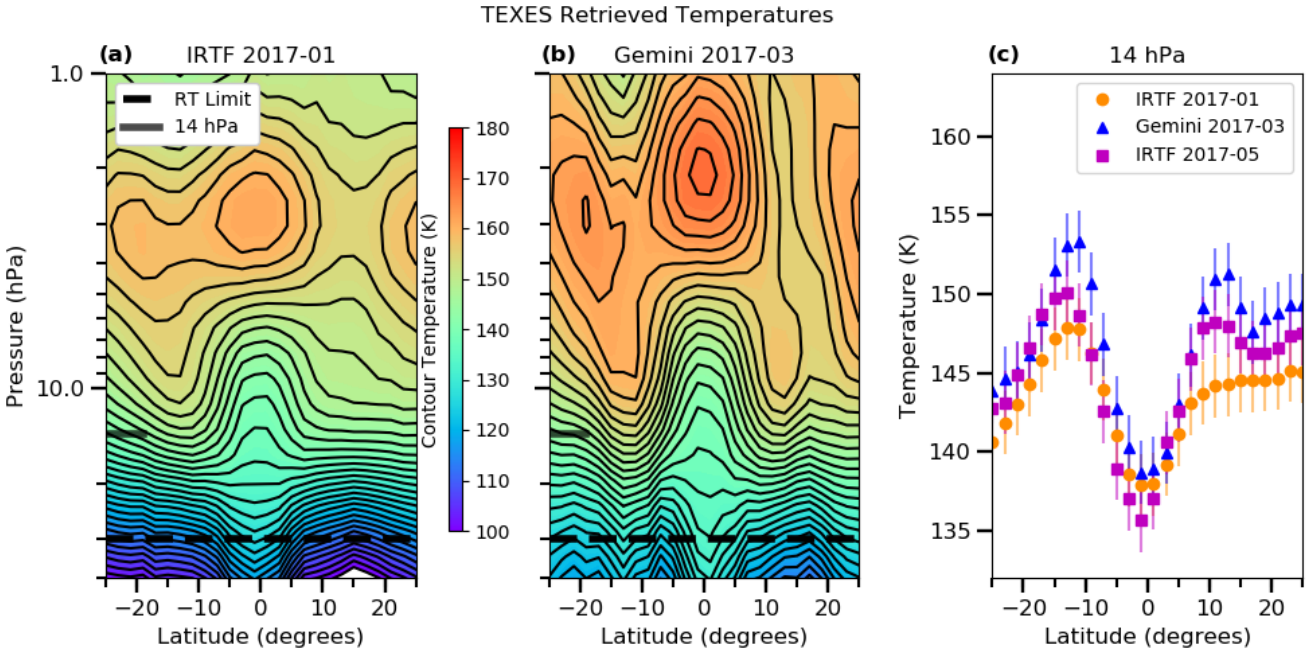

Figure 3: Retrieved temperatures of the QQO equatorial minimum between for IRTF/Gemini observations. Surface contours in panels (a-b) are every 2 K with a common color bar. The dashed black line at 30 hPa represents the high pressure limit of retrievals within the 2 K estimated uncertainty. Horizontal ticks at 14 hPa on the left axis in panels (a-b) correspond to the pressure level for temperature profiles shown in panel (c).

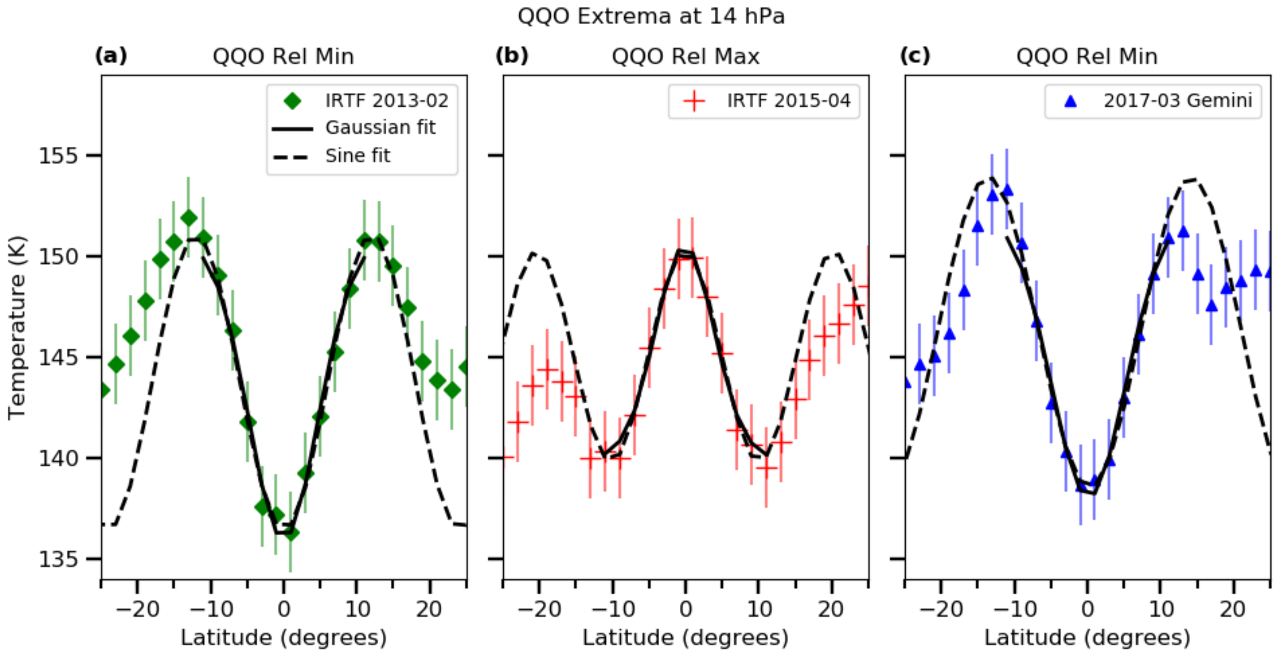

Figure 4: Gaussian (solid) and Sinusoidal (dashed) fits at 14 hPa for different QQO extrema. Fits apply to data spanning ±11°.

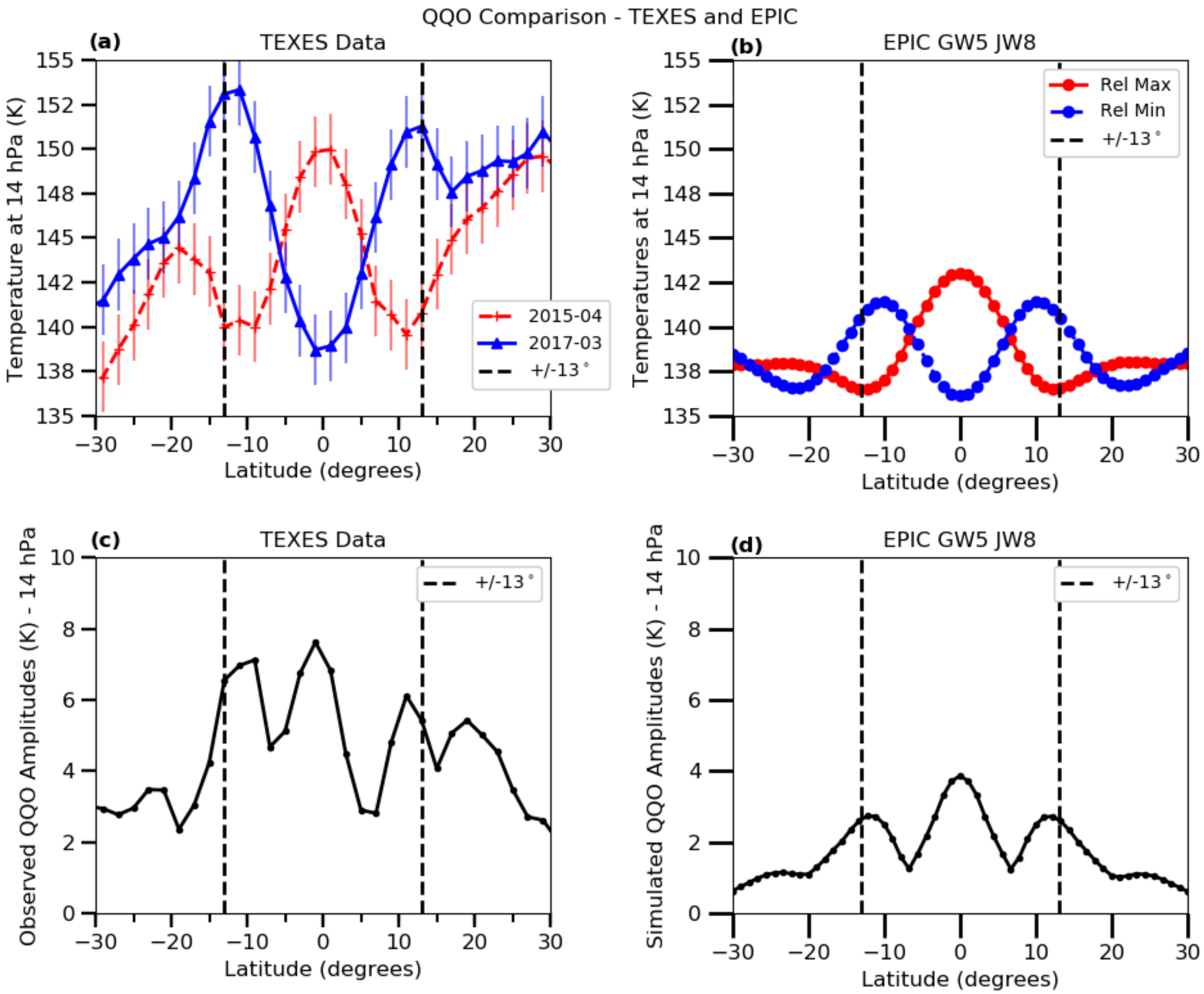

Figure 5: Panel (a) shows TEXES observations of the QQO at opposite phases, while panel (c) shows temperature amplitudes with latitude. Panel (b) is similar to (a) but is shown for a QQO simulation, with the modeled QQO amplitudes shown in panel (d). Vertical lines at ±13° are shown in each panel.

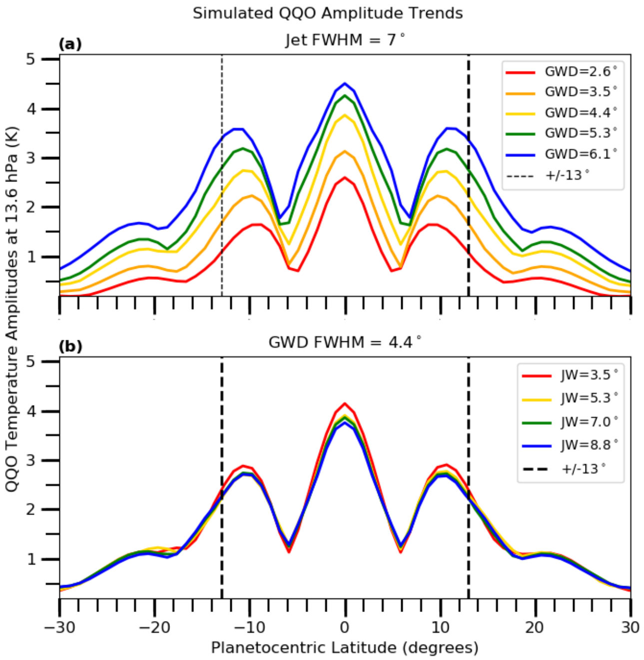

Figure 6: Panel (a) shows the effect of changing the FWHM of the GWD on QQO temperature amplitudes while panel (b) shows there is virtually no effect on changing the FWHM of the QQO jet. The QQO temperature amplitudes y-axis label applies to both panels. The vertical dashed lines show the observed anti-correlated QQO temperature amplitude location at ±13°. All latitudes are in planetocentric coordinates.

Table 1
Temperature Fits Between 11–16 hPa

Telescope Date	Fit Method	11 hPa (Degrees)	14 hPa (Degrees)	16 hPa (Degrees)
IRTF 2013-02	Sine [$\lambda/2$]	14.2	12.0	11.5
	Gaussian [FWHM]	12.1	11.1	10.7
IRTF 2015-04	Sine [$\lambda/2$]	10.2	10.1	10.4
	Gaussian [FWHM]	9.6	9.4	9.6
IRTF 2017-01	Sine [$\lambda/2$]	14.0	13.7	26.4
	Gaussian [FWHM]	11.6	11.5	12.6
Gemini 2017-03	Sine [$\lambda/2$]	13.6	13.9	15.6
	Gaussian [FWHM]	11.8	11.9	12.4
IRTF 2017-05	Sine [$\lambda/2$]	12.0	11.3	10.6
	Gaussian [FWHM]	11.0	10.5	10.0
IRTF 2017-07	Sine [$\lambda/2$]	12.3	11.8	11.2
	Gaussian [FWHM]	10.9	10.6	10.1
STD DEV	Sine [$\lambda/2$]	1.5	1.5	6.2
STD DEV	Gaussian [FWHM]	0.9	0.9	1.3

Table 1: The domain of data used for reported fit results in this table were ±11° latitude. These results typically varied by less than ∼1° for domains of ±9° and ±13° latitude, which we estimate is our approximate uncertainty in the fitting methods to the TEXES data and similar to the calculated standard deviation.

Appendix A. Additional Analysis

Figure A.1 shows meridional profiles for retrieved temperatures for Gemini and IRTF observations in 2017 at several pressures. These pressures span the range of the QQO equatorial relative minimum phase and all of the profiles have a similar equatorial structure to those shown in Figure 3 panel (c). Figure A.1 displays the temperatures over a larger latitude domain which shows there are differences in observational structure away from the equator and a north-south asymmetry. The is also a slight increase seen at all latitudes of the Gemini measured temperatures relative to the IRTF measurements and is likely due to the different foreoptics used within TEXES to couple the two different telescopes. Slight differences in cold stop filling factors can lead to small shifts in the calibration given that our radiometric blackbody calibration is necessarily inserted into the instrument line of sight after the telescope. The vertical translation of the retrieved temperatures, most prominent at 11 hPa in Figure A.1, had no significant impact on the analysis of the meridional structure presented in the main body of the paper.

The sine curve half-wavelengths occasionally do not converge on meridional widths that resemble surrounding calculations, but this behavior is not observed for fitting a Gaussian. We believe the sine curve does not fit transitions between QQO relative extrema phases because a flattened temperature profile might result in a very large half-wavelength, while the Gaussian FWHM appears more easy to constrain. We did not vary initial values in our curve fitting analysis for individual observations, but kept them constant. Figure A.2 shows only a few sine curve fitted widths measure extremely large widths that all occur during QQO extrema phase transitions. It might be possible to extract vertical wind structure by analyzing the thermal wind relation at the equator with more complicated analyses presented in Marcus et al. (2020) and systematically studying initial conditions of TEXES temperature retrievals. The strong prograde jets at 7°S, 7°N, and 24°N would be ideal candidate areas to investigate because their high velocities make them likely to have gradual decreases in the vertical direction according to stability arguments.

Figure A.3 shows that the equatorial temperature amplitudes increased as the FWHM of the GWD was increased and that the QQO temperature amplitude is largely independent of the initialized jet FWHM. The cases with a GWD FWHM of $\leq 2°$ did not produce simulations with a QQO. Cases that had GWD FWHM $\geq 8°$ did not produce a stable QQO within the model and are not shown. Simulations that were unstable are shown with hollow symbols in Figure A.3 and shows the limitations of EPIC to model the QQO such that we could not increase the GWD and simultaneously maintain numerical stability.

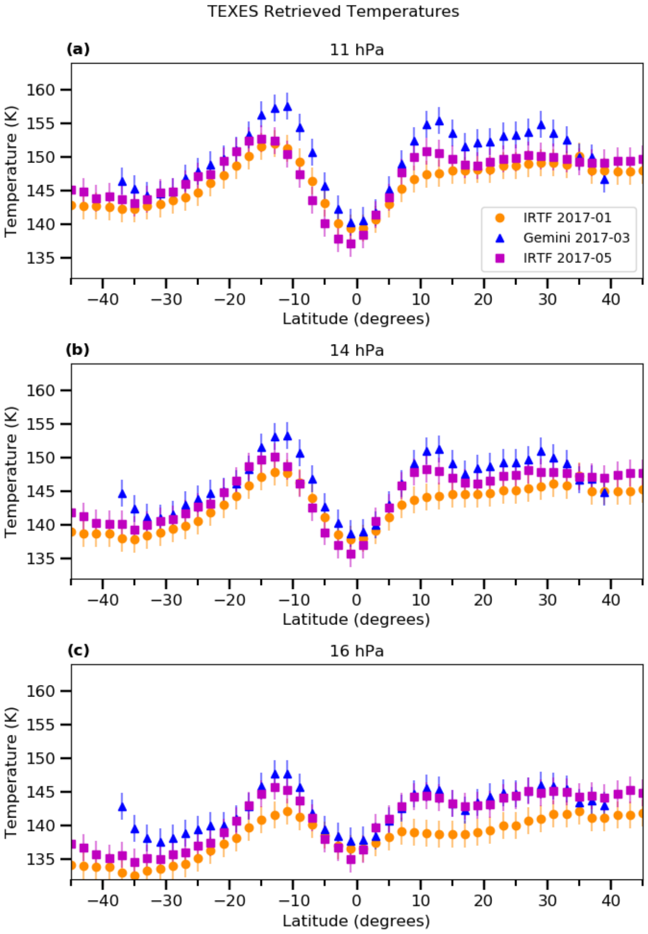

Figure A.1: Meridional temperature profiles for 2017 observations at IRTF and Gemini telescopes.

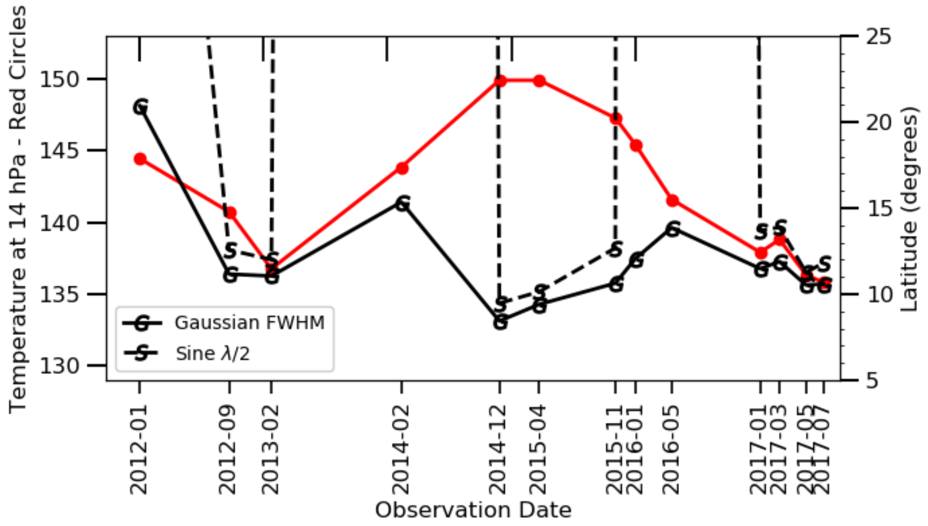

Figure A.2: Meridional widths calculated from both the sine curve half-wavelengths (S symbol dashed line) and Gaussian FWHM (G symbol solid line).

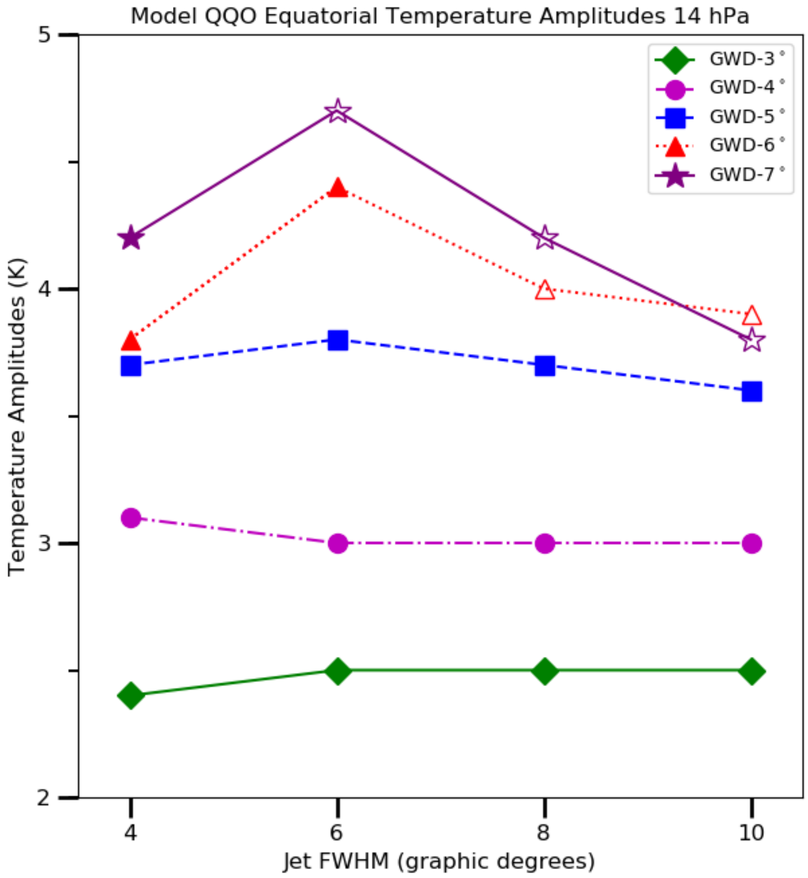

Figure A.3: Equatorial temperature amplitudes at 14 hPa in simulations exploring the initial jet and GWD parameter space. The FWHMs for GWD and QQO jet width are in planetographic degrees latitude. Unstable simulations that did not develop multiple stable QQO cycles are indicated by hollow symbols.